WALL-RESOLVED iLES OF COMPRESSOR TANDEM-BLADES USING HIGH-ORDER DG METHOD

Andrea Rocca[1,†,*], Michel Rasquin[1], Koen Hillewaert[1,2], Anis Al Rifai[3], Thomas Toulorge[1]

[1]Cenaero, Charleroi, Belgium
[2]University of Liège, Liège, Belgium
[3]Safran Aero Boosters, Herstal, Belgium

ABSTRACT

The purpose of outlet guide vanes in low-pressure compressors is to redirect the incoming airflow axially. As climate, energy, and environmental goals push for greater efficiency, there is increasing pressure to enhance the performance of modern aeronautical engines, resulting in more extreme flow conditions. However, high flow turning often leads to increased losses and a higher risk of flow separation. Tandem blade designs offer a solution by enabling large flow deviations while helping to maintain flow attachment. This is achieved by making the boundary layer on the rear blade more resilient to separation. Despite these benefits, tandem blade configurations are subject to complex flow phenomena, including interactions between the wake of the front blade and the boundary layer on the suction side of the rear blade, laminar separation bubbles on the front blade, laminar-to-turbulent transition, as well as turbulent mixing and merging of the wakes. These effects significantly influence performance and pose challenges for standard RANS models. This paper investigates the performance of tandem blades using wall-resolved Large-Eddy Simulations (wrLES), offering a detailed comparison with RANS results. Specifically, we present wrLES of a low-pressure compressor tandem blade in a cascade configuration, employing a high-order discontinuous Galerkin method (DGM) to capture the complex flow dynamics.

Keywords: Tandem-Blades, LES, RANS, Compressor, DG method

NOMENCLATURE

Acronyms

BH	Boussinesq Hypothesis
DNS	Direct Numerical Simulation
NSs	Navier Stokes Equations
RANS	Reynolds-Averaged Navier-Stokes Simulation
RS	Reynolds Stress
RST	Reynolds Stress Tensor
wrLES	Wall-Resolved Large Eddy-Simulation
WBLI	Wake- Boundary Layer Interaction

[†]Joint first authors
[*]Corresponding author: andrea.rocca@cenaero.be
Documentation for `asmeconf.cls`: Version 1.38, October 16, 2025.

1. INTRODUCTION

Sustainability targets in aviation require radical innovation in engine design. In particular, engine manufacturers aim to improve performance. To reach that goal, tandem blades are innovative geometries able to guide the flow into greater turns with reduced losses compared to single blades. For this reason, they are good candidates to replace highly loaded axial compressor outlet guide vanes. This configuration, together with extreme flow conditions, challenge the standard Reynolds Averaged Navier-Stokes Simulations (RANS) simulation tools.

In tandem blades, the wake generated by the front blade plays an active role in aerodynamic performance and should not be considered merely an unavoidable or undesired byproduct of fluid-structure interaction. The interaction of the two wakes, along with the wake-boundary layer interaction and more classical phenomena such as flow separation, reattachment and eventually transition, are key elements that make this case worthy of attention. Additionally, the design process becomes more complex as it involves two blades and additional geometrical parameters, such as axial overlapping, gap, and pitchwise distance. Moreover, transitioning from a single blade to a tandem blade introduces a new degree of freedom, as the front blade could be designed to allow rotation, enabling it to comply with the operating point and thereby increasing both the design's complexity and its potential.

To ensure the reliability of RANS methodologies used for design, scale-resolving simulations, such as the direct solution of the compressible Navier-Stokes equations (DNS) and wall-resolved Large-Eddy simulation (wrLES), supported by experiments, provide reliable and comprehensive reference results. A DNS is the most accurate technique but remains unfeasible for most flows in the turbulent regime, since the computational cost increases as $Re^{3.5}$ in wall-bounded turbulence (Re is the Reynolds number of the flow), as shown for example in [1]. The computational cost required to solve the boundary layer using LES grows as $Re^{2.5}$ (see [2]), is slightly lower than that of a DNS, but remains highly expensive.

Scale-resolving simulations give access to all information

needed for performance assessment, but are still not suitable for design and optimization due to their computational cost. However, these methods can be used for the assessment of RANS models based on high-fidelity results, possibly assisted with machine learning techniques ([3, 4]). However, AI-CFD tools are still not mature, and the training of models requires also an important effort, without the guarantee that the trained model will generalize to all flow conditions. Computational cost and numerical convergence difficulties have hindered the popularity of higher-order closures such as Reynolds Stress Transport and nonlinear eddy viscosity. On the other hand, design engineers face the challenge of enhancing the already high performance under increasingly extreme flow conditions, relying on turbulence models developed decades ago. For this reason, it is crucial to have a reliable and detailed assessment of the validity range of RANS models. This is possible by leveraging uncertainty quantification tools [5] and advanced visualization techniques.

Recent literature on tandems is focused on the study of secondary flows [6], generated by the blades themselves or by the end-walls. Most of it consists in experimental works and numerical RANS simulations [7–10].

In this work, we present wall-resolved Large-Eddy Simulations (wrLES) of a low-pressure compressor tandem blade in cascade configuration using a high-order discontinuous Galerkin method (DGM) [11]. The Navier-Stokes equations are solved directly without employing sub-filter scale (SFS) models. Instead, the numerical scheme inherently dissipates scales smaller than the grid resolution. This built-in dissipation defines the implicit nature of the simulation, which is often referred to as Implicit Large-Eddy Simulation (iLES). In iLES, the numerical discretization itself acts as the sub-filter scale model, removing the need for explicit SFS modeling. Hereinafter we will simply refer to wrLES. The flow is subsonic. The simulations are carried out using the solver Argo [12], developed at Cenaero. To the best of our knowledge, this is the first numerical work carried out using high-order wall-resolved LES on this specific type of blade configuration. We seek to produce high-quality and comprehensive reference data for a subsonic tandem blade cascade flow and exploit it to benchmark several RANS turbulence models by performing simulations with the open-source toolkit SU2 [13].

The paper is organized as follows. Section 1 introduces the case to the reader and presents the numerical setup for both wrLES and RANS simulations. Sections 2 and 3 describes the methodology for the wrLES and the RANS, respectively. Section 4 presents the results, focusing initially on performance-based engineering quantification and then progressing to turbulence-related metrics. The discussion extends to more advanced topics, such as verifying the validity of the Boussinesq hypothesis of linear eddy viscosity and analyzing the state of turbulence. This analysis naturally leads to exploring turbulence perturbations in RANS simulations and the application of uncertainty quantification, utilizing SU2's native tools. This study emphasizes the significance of this type of analysis, demonstrating that valuable, engineering-relevant insights can still be extracted from RANS models. Finally, the conclusions summarize the key findings and implications of this work.

2. APPLICATION CASE AND NUMERICAL SETUP

The cascade is modeled as a bi-periodic (pitch and span) problem. The Reynolds number based on the total chord C is $Re_c = 300,000$; the expected inlet Mach number is $Ma_i = 0.6$. The fluid is air, modeled as a perfect gas. The dynamic viscosity is determined using Sutherland's law. Total quantities and flow direction are imposed at the inlet, while a static pressure is imposed at the outlet. No-slip and adiabatic conditions are enforced on the blades. The flow is homogeneous and periodic along the spanwise direction (z coordinate), while it is periodic in the pitchwise direction (y coordinate). The flow is considered initially laminar since no turbulence is injected. Turbulent inflow will be considered in future works.

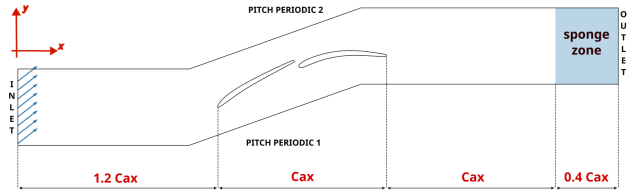

FIGURE 1: THE COMPUTATIONAL DOMAIN

Figure 1 shows the computational domain. It extends for 3.5 total axial chords C_{ax}. Starting from 1.0 C_{ax} from the trailing edge (TE) of the rear blade (RB), a sponge zone is applied to avoid spurious back-reflections of acoustic waves from the outlet and smooth-out the wake's turbulence. The span length is 12% $C_{\text{ax, fb}}$, which corresponds to 1/11 of the pitch. As an example, Figure 2 shows the two-point correlations ρ_{ii} (following Pope's definition [14]), as defined in Equation 1, on the suction side of the front and the read blades (indicated by the red dots in the top panel).

$$\rho_{ii}(z, \mathbf{x}, t) = \frac{\overline{u_i(\mathbf{x}, t)\, u_i(\mathbf{x} + z, t)}}{\overline{u_i(\mathbf{x}, t)\, u_i(\mathbf{x}, t)}} \tag{1}$$

Taking advantage of the symmetry of ρ_{ii} w.r.t. the span direction, the bottom panel is divided into two parts, left and right. On the left, ρ_{ii} is shown for the front blade in the interval z/span < 0.5. The rear blade is considered for the interval z/span > 0.5 and is shown on the right-hand side. Probes are placed 15 wall units from the walls. One wall unit ($n^+ = 1$, where n indicates the local wall-normal coordinate) corresponds to a distance from the wall defined as:

$$d = \frac{\mu}{\sqrt{\tau_w \rho}}. \tag{2}$$

In particular d is the distance of the first degree of freedom (dof) off the wall for n^+ and the distance between two successive dof in the wall-tangent directions to evaluate Δs^+ and Δz^+. In other words, these resolutions correspond to the mesh resolution divided by the polynomial order p. This analysis was repeated on both the pressure and suction sides of the two blades, as well as in the wake, consistently confirming the suitability of the span selection. A second-order unstructured (hexa-dominant) 2D mesh is generated and extruded in the spanwise direction using the open-source mesh generator Gmsh [15]. It is composed of

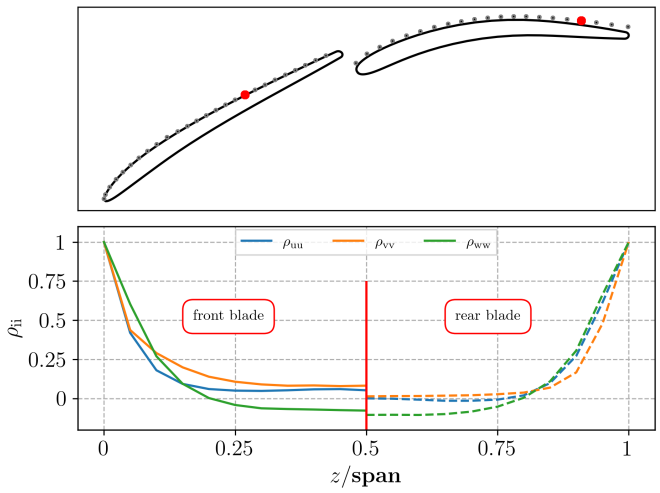

FIGURE 2: TWO-POINTS CORRELATION FUNCTION

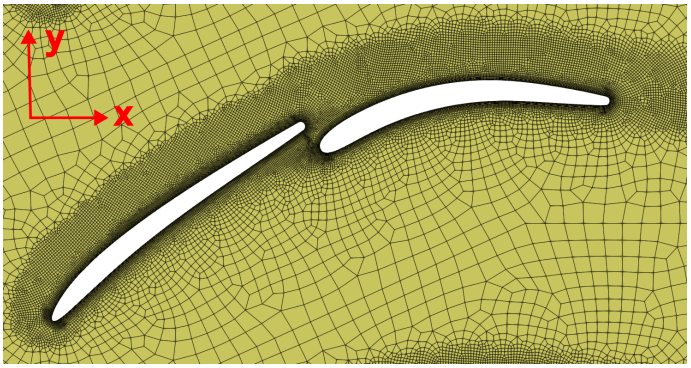

FIGURE 3: COMPUTATIONAL GRID

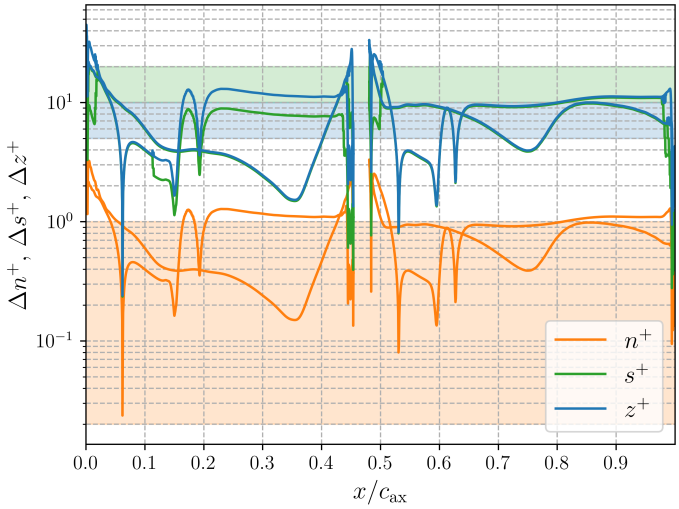

FIGURE 4: WALL RESOLUTION

440,000 cells. The high-order solution employs a third-order polynomial which yields a fourth-order accurate scheme, with 30×10^6 degrees of freedom per equation. The grid is shown in Figure 3. The visualization is three times coarser than the actual discretization of the solution is because third order polynomials $p3$ are used to represent the solution within each cell. On the front and rear blades (see Figure 4), the resolution follows the usual guidelines for wrLES, with $n^+ < 1$ (orange), $s^+ < 25$ (green) and $z^+ < 25$ (blue), where n^+, s^+, z^+ are respectively the local wall-normal, (streamwise) wall-tangential and spanwise coordinates, expressed in wall-units (see equation 2). To emphasize the high degree of spatial accuracy, the ranges that satisfy the DNS requirements [2], namely $n^+ < 1$, $10 \leq s^+ \leq 20$, and $5 \leq z^+ \leq 10$, are highlighted.

The solution algorithm advances in time using an implicit second-order Backward Differentiation Formula scheme, with a time step size of 10^{-7}s.

Statistics are collected over 22 convective time units, based on the inlet velocity and the total axial chord. The time-averaged data are further processed using spanwise averaging. Averaged quantities are indicated by the overline symbol $\overline{\bullet}$.

3. RANS SIMULATIONS

A RANS simulation campaign has also been performed using the open-source code *SU2* (8.1.0). The results obtained with two turbulence models are presented hereafter: i) the Shear Stress Transport (*SST*) two equations model, and ii) the transitional model $SST - \gamma - Re_\theta$, four equations closure, of Menter and Langtry [16, 17]. The SST model is the version labeled 2003*m* in the NASA Turbulence Modeling Resource [18], where 2003 refers to the year in which the paper [19] was published and the letter *m* stands for "*modified*", hence the turbulent kinetic energy k is excluded from the production term $\mathcal{P}_k$ of the turbulent kinetic energy transport equation. The fluid properties and the boundary conditions match those of the wrLES, except for the fact that the RANS domain is purely bi- dimensional. The mesh is composed of about 50.000 quads and is similar to the one employed in the LES, with the exception that the cell size is relaxed in the direction tangent to the blade. The wall-normal distance of the first cell layers adjacent to the blades yields $n^+ < 1$. Before selecting the final mesh, a grid refinement study has been performed. Inlet conditions for turbulent quantities are turbulence intensity $I = 0.5\%$ and viscosity ratio $\mu/\mu_t = 10$. Numerical schemes utilized are Green-Gauss for the approximations of gradients and Roe's flux combined with MUSCL reconstruction (second order upwind) for the convective terms. Turbulence convection terms are interpolated with a first order upwind scheme. The iterative solver is the restarted FGMRES.

4. RESULTS AND ANALYSIS

4.1 Flow description and pressure distribution

Using a specific ParaView plugin to visualise high-order fields generated by the Argo solver [20], complex physical phenomena occurring in the flow are revealed. These are illustrated in Figure 5, where the instantaneous quantity $\nabla\rho/\rho$ is employed to provide a qualitative overview of the flow dynamics. We observe laminar bubbles detach from the leading edge of the front

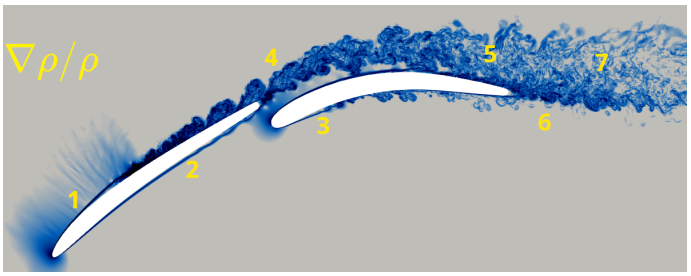

FIGURE 5: TURBULENT FLOW VISUALIZATION USING $\nabla\rho/\rho$

blade, leading to separation-induced transition on both the pressure side and suction side of the front blade (marked with numbers 1 and 2 on Figure 5), and on the pressure side of the rear blade (3). In a tandem blade configuration, the wake of the front blade (4) plays a crucial role by constraining the flow that accelerates through the passage between the two blades. This prevents flow separation on the suction side of the rear blade, enabling an increased load on the blade. In this particular setup, where the gap is relatively short, the wake of the front blade interacts with the boundary layer on the suction side of the rear blade (4), governing the transition mechanism, which tends to by-pass turbulence transition [21]. Subsequently, the two wakes (3, 6) spread and merge downstream (5). The bifurcation of the front blade wake is shown in (7). A comparison of the averaged Mach number for the wr-LES and $SST-\gamma-\mathrm{Re}_\theta$ is shown in Figure 6. The two solutions are qualitatively undistinguishable. Figure 7 presents

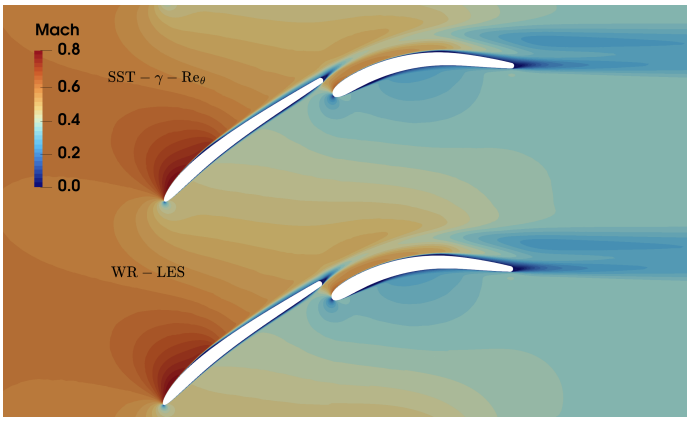

FIGURE 6: MACH NUMBER COMPARISON

the pressure ratio, π, and the angle between the velocity vector and the horizontal axis, α, along a streamline passing through the mid-channel for the wrLES. With a turning of 55° degrees, the tandem configuration achieves a flow compression of approximately 17%.

4.2 Turbulent BL and wake analysis

Continuing with the analysis of the two blades,Figure 8 illustrates the isentropic Mach number from LES alongside the RANS results. The isentropic Mach number, M_{is}, is defined as:

$$M_{is} = \sqrt{\left[\left(\frac{p_t^i}{p}\right)^{\frac{\gamma-1}{\gamma}} - 1\right]\frac{2}{\gamma-1}}, \tag{3}$$

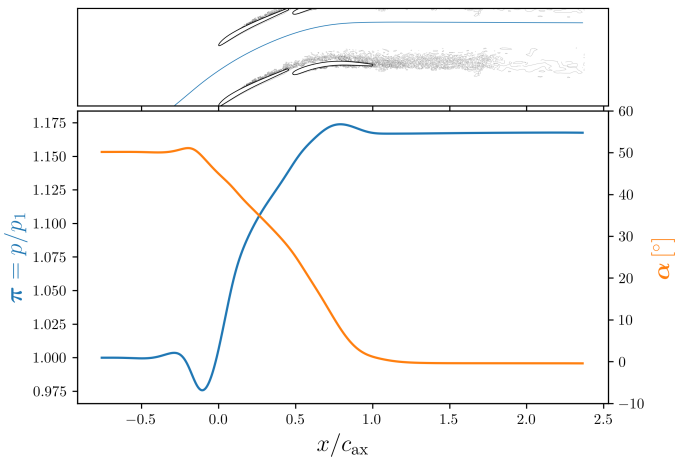

FIGURE 7: STREAMLINES ANALYSIS

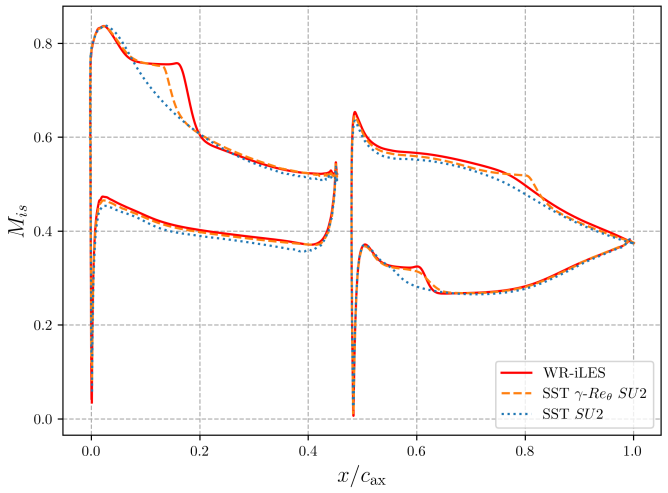

FIGURE 8: ISENTROPIC MACH NUMBER

where p_0^i is the total pressure imposed at the inlet and $\gamma = 1.4$. At $x/\mathrm{C_{ax}} = 0$ the three curves overlap, indicating consistent Mach number at the inlet across the three simulations. On the suction side of the front blade the $\mathrm{SST}-\gamma-Re_\theta$ turbulence model qualitatively captures flow separation, unlike the standard SST model, which proves unsuitable for the present flow conditions. A similar observation applies to the pressure side of the rear blade. However, on its suction side, the semi-empirical nature of the $\mathrm{SST}-\gamma-Re_\theta$ model might not account for the unsteady wake-boundary layer interaction and, instead, it predicts a laminar boundary layer separation, reattachment, and transition to turbulence, as it did for the front blade. These uncertainties significantly influence the flow evolution downstream, highlighting the limitations of the turbulence models under the analyzed conditions. For example, RANS models predict an exit flow angle of almost 1.5° pointing upward, while wrLES predicts a slightly negative flow angle. As already mentioned in Figure 5, the wake of the front blade interacts with the boundary layer developing on the suction side of the rear blade. Turbulent transport of

momentum towards the blade is governed by the off-diagonal components of the Reynolds Stress Tensor (RST), in particular $\overline{u'v'}$. Figure 9 (a) shows the contour plot of k/U_∞^2. The RST and k are sampled at 5 locations indicated with the locally wall-normal lines colored by red, pink, green, yellow and blue respectively. It is subsequently rotated to align with the local reference frame $\rho - \theta$. Each ρ-axis is aligned with the respective line and points outward. The segments have all the same length. In Figure 9 (b), $-\overline{\partial u'v'}/\partial r$ is shown against the normalized non-dimensional local-radial coordinate, $r^\star$. It is plotted with solid lines and the values are shown on the bottom x-axis. On the same plot is shown the turbulent kinetic energy, made non-dimensional with a velocity scale U_∞^2. It is represented using a dashed line and refers to the top x-axis. Moving from the first location on the left, characterized by the red color, to the last one on the right, we notice that the anisotropy term transports momentum from the wake of the front blade towards the rear blade suction side, determining in this way a different dynamics than for isolated blades. When $-\overline{\partial u'v'}/\partial r$ assumes negative values, the Reynolds stress subtracts momentum from the mean field towards the fluctuating one, thus retarding the transition (the same term appear with opposite sign in the equation for the fluctuating field which can be obtained by subtracting from the NSs the Reynolds-averaged NSs [14]). At the same time the wake spread and the k profile flattens. The turbulent kinetic energy diffused into the boundary layer determines a by-pass like transition to turbulence [21].

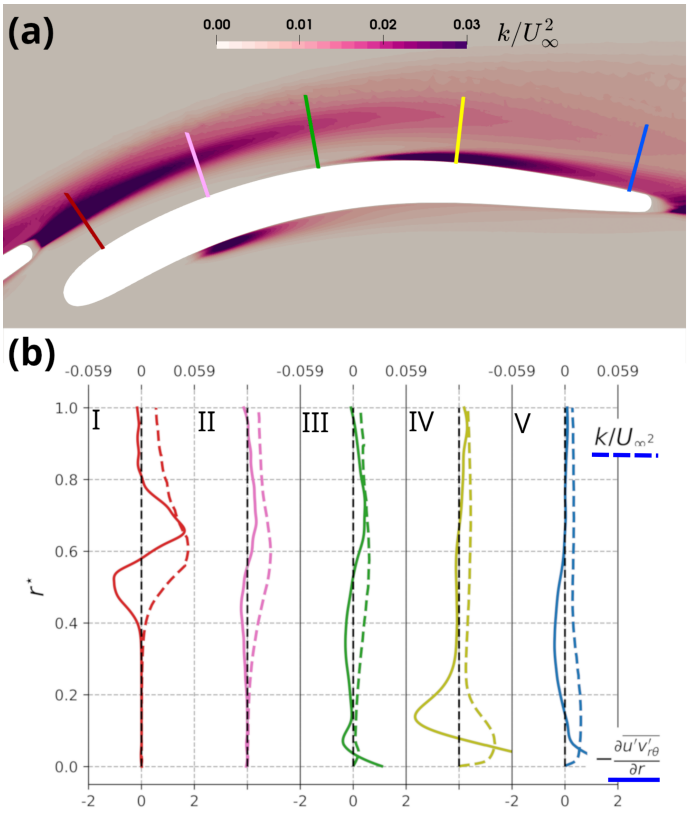

FIGURE 9: WAKE-BL INTERACTION

Figure 10 shows the loss coefficient ω, along the non-dimensional pitch-coordinate, η. They are defined as:

$$\omega = \frac{p_t^i - \overline{p_t(\eta)}}{p_t^i - \overline{p_s^i}} \tag{4}$$

$$\eta = \frac{y - min(y)}{\text{pitch}} \tag{5}$$

where p_t^i correspond to total pressure prescribed at the inlet, $\overline{p_s^i}$ is the time- and span-averaged static pressure at the inlet, $\overline{p_t(\eta)}$ is the time- and span-averaged total pressure at $x = 0.35\,\text{Cax}$ downstream the TE of the rear blade. For a tandem configuration,

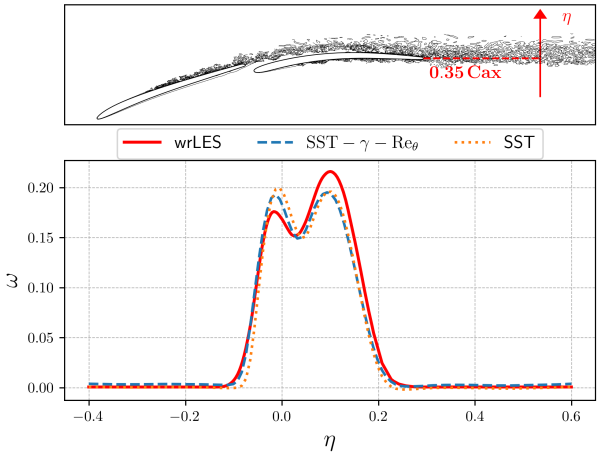

FIGURE 10: WAKE LOSSES

the total pressure loss curve exhibits a two-humped shape, where the humps correspond to the wakes. The wrLES simulation predicts an asymmetric profile with higher losses originating from the pressure sides of the blades. The local minimum is slightly shifted to a positive η. The second maximum appears at $\eta < 0$, reflecting additional losses from the pressure sides.

In contrast, both RANS models predict lower losses on the suction side and higher losses on the pressure side, resulting in a quasi-symmetric ω. The discrepancies between these methods are closely tied to differences in the mechanisms of turbulent kinetic energy production and dissipation. Figure 11 shows a comparison of the non-dimensional turbulent kinetic energy, k/U_∞^2, between the wrLES and the two RANS models. Both RANS models underestimate k. In the standard SST the production of k starts much closer to the LE compared the other two cases, but it remains relatively low. The Langtry-Menter model correctly predict zero k until approximately separation, with a sharp increase there. To better understand this behavior, it is useful to consider the expression for the turbulent kinetic energy production term:

$$\mathcal{P}_k = \overline{u_i' u_j'}\,\overline{S}_{ij} = 2\mu_t \overline{S}_{ij}\overline{S}_{ij}, \qquad \text{SST} \tag{6}$$

$$\hat{\mathcal{P}}_k = \gamma_{\text{eff}}\,\mathcal{P}_k, \qquad \text{SST} - \gamma - \text{Re}_\theta \tag{7}$$

where $\gamma_{\text{eff}} = \max(\gamma,\ \gamma_{\text{sep}})$ is shown in Figure 13. In this formulation, Einstein summation notation is used, implying summation

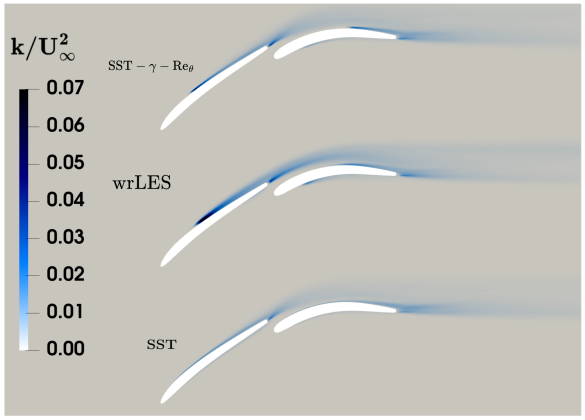

FIGURE 11: NON-DIMENSIONAL TURBULENT KINETIC ENERGY COMPARISON

over repeated indices. The influence of γ_{eff} in driving the turbulence production and thereby defining the turbulent kinetic energy field is clearly evident. The relative error E_k committed by the SST-γ-Re$_\theta$ in the evaluation of k is illustrated in Figure 12.

$$E_k = \frac{k_{\text{wrLES}} - k_{\text{RANS}}}{k_{\text{wrLES}}} \times 100 \tag{8}$$

In this case, the mean rate of strain does not appear to be a suitable approximation for the Reynolds stresses, resulting in an underestimation of the turbulent kinetic energy production.

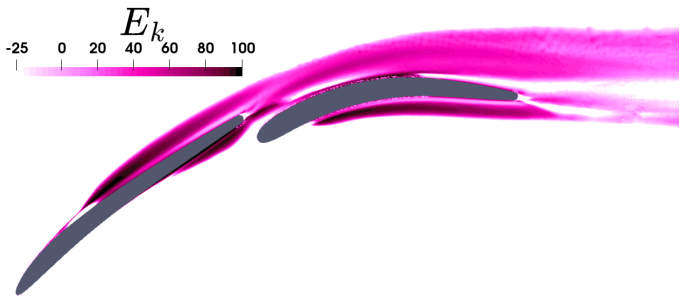

FIGURE 12: TURBULENT KINETIC ENERGY ERROR %

4.3 Assessment of the Boussinesq approximation

In this section, we delve deeper into the possible reasons behind the misalignment between RANS and LES results, focusing specifically on the application of tandem blades. By now, the reader should be familiar with the flow characteristics, which exhibit significant complexity due to the multitude of interacting phenomena, even at design conditions.

The limitations of RANS turbulence modeling are well-known, particularly in the context of accurately capturing such intricate flows. To enhance our understanding not only of the underlying physics but also of the predictive tools used in engineering design, it is valuable to examine the validity of the Boussinesq Hypothesis (BH) of linear eddy viscosity, which assumes linearity between the Reynolds stresses $\overline{u_i' u_j'}$ and the mean

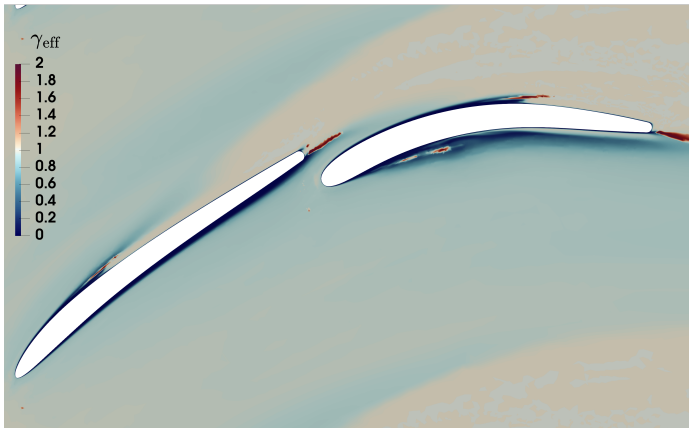

FIGURE 13: LANGTRY-MENTER'S γ_{eff}

strain rate tensor $\overline{S_{ij}}$. This hypothesis forms the cornerstone of most commonly used turbulence models, yet its assumptions may contribute to the observed discrepancies between RANS and LES predictions. The BH asserts that:

$$-\rho\,\overline{u'_i u'_j} = 2\,\mu_t \left(\overline{S}_{ij} - \frac{1}{3}\frac{\partial U_k}{\partial x_k}\delta_{ij} \right) - \frac{2}{3} k \rho \delta_{ij}, \tag{9}$$

where the mean strain rate tensor is defined as

$$\overline{S}_{ij} = \frac{1}{2}\left(\frac{\partial U_i}{\partial x_j} + \frac{\partial U_j}{\partial x_i} \right), \tag{10}$$

and where $k = \frac{1}{2}\overline{u'_i u'_i}$ is the turbulent kinetic energy.

One approach to verify the hypothesis is to normalize the tensor contraction between the traceless anisotropic part of the Reynolds stress, $\overline{R}_{ij}$, and the mean strain rate [22]. The resulting scalar field, ρ_{RS}, lies in the range [0, 1] and is derived from the anisotropic stress tensor:

$$\overline{R}_{ij} = \rho\,\overline{u'_i u'_j} - \frac{2}{3}\rho\, k \delta_{ij}. \tag{11}$$

Using the Frobenius inner product (:), ρ_{RS} is expressed as:

$$\rho_{RS} = \frac{|\overline{R}_{ij} : \overline{S}_{ij}|}{||\overline{R}_{ij}||\,||\overline{S}_{ij}||}, \tag{12}$$

where the operation $||\overline{A}_{ij}|| = \sqrt{|\overline{A}_{ij} : \overline{A}_{ij}|}$. For $\rho_{RS} = 1$ the eigenvectors of the two tensor are aligned and BH behind two equations RANS closure is valid.

Figure 14 shows ρ_{RS}, specifically where $\rho_{RS} > 0.86$. Since the inflow is laminar, the analysis is only valid within turbulent boundary layers and wakes.

4.4 Barycentric map

The coupling between the previous analysis with the characterization of the turbulence anisotropy state provides deeper insights into the underlying flow dynamics. In the same spirit of Lumley [23], Banerjee proposed a barycentric representation [24]. This latter invariant map is a linear representation that weighs the different limiting states of turbulence anisotropy

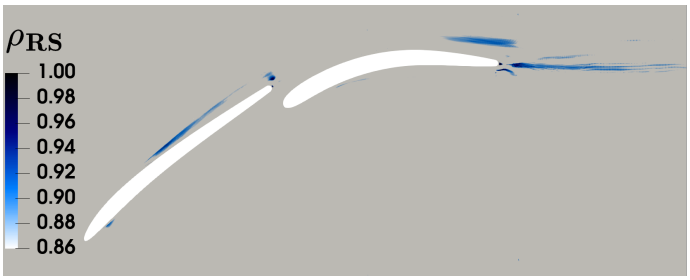

FIGURE 14: VALIDITY OF THE LINEAR EDDY-VISCOSITY HYPOTHESIS

equally. The limiting states are placed at x_{1C}, x_{2C}, and x_{3C}, which represent the corners of the equilateral triangle, and hence the coordinate system of the barycentric map (x_B, y_B) is defined such that:

$$x_B = C_{1c}\, x_{1c} + C_{2c} x_{2c} + C_{3c} x_{3c} \tag{13}$$

$$y_B = C_{1c} y_{1c} + C_{2c} y_{2c} + C_{3c} y_{3c} \tag{14}$$

with the corresponding weights (C_{ic}) determined by the eigenvalues $(\lambda_1 \geq \lambda_2 \geq \lambda_3)$ of the normalized Reynolds stress anisotropy tensor:

$$a_{ij} = \frac{\overline{R}_{ij}}{2k}, \tag{15}$$

such that:

$$C_{1c} = \lambda_1 - \lambda_2, \tag{16}$$

$$C_{2c} = 2(\lambda_2 - \lambda_3), \tag{17}$$

$$C_{3c} = 3\lambda_3 + 1. \tag{18}$$

Since the eigenvalues sum to zero, the weights also sum to zero, enabling a direct mapping to an RGB (or HSV) color scheme for enhanced visualization of anisotropy [25]. Consequently, one-component turbulence is represented in red, two-component turbulence in green, and isotropic turbulence in blue, with all other states appearing as blends of these primary colors within the map (the barycentric map is shown in Figure 15(a) at the right bottom corner).

Figure 15(a) depicts the state of turbulence in the tandem blade, comparing results from the transition model and wrLES. Additionally, Reynolds Stress are extracted from the wake (red vertical arrow for wrLES and orange for RANS) and along a streamline. The evolution of the turbulence state in the wake is shown in Figures 15 (b) for both wrLES and RANS. The color map indicates the normalized pitch position, y^*. RANS data are placed along the plain-strain turbulence. Figures 15 (c) present a similar analysis along a streamline, but only for the wrLES. The streamlines originates close to the leading edge. s/L is the non-dimensional distance from the beginning of the streamline, as shown in Figure 15(a), and the color map is customized in order to link the white color to the position of the trailing edge of the rear blade. From there on there is no significative change and the red markers are all clustered close each other. The analysis highlights two key observations:

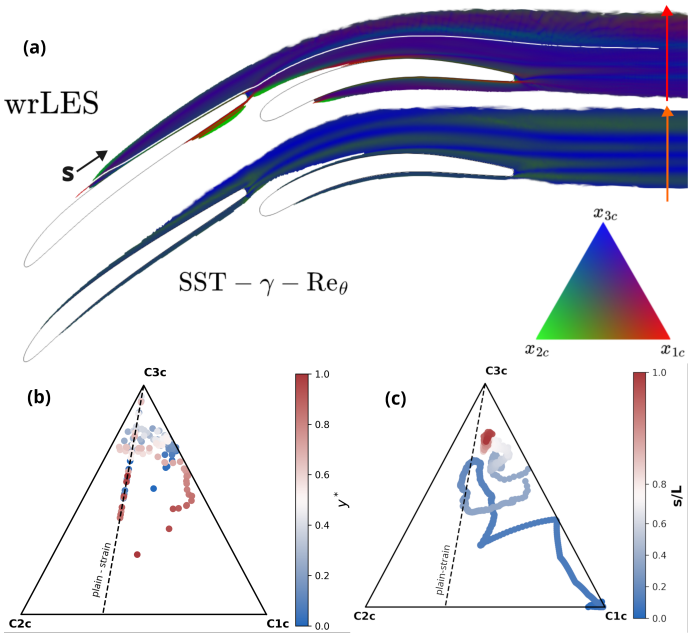

FIGURE 15: BARYCENTRIC ANALYSIS IN THE WAKE AND ALONG A STREAMLINE

- The SST model generally predicts turbulence as either isotropic or plane-strain (along the dashed line). In contrast, scale-resolving LES demonstrates that, within the wake, the turbulence more closely approaches an axisymmetric expansion limit state (1C $\Rightarrow$ 3C). The Reynolds stress tensor (RST) evolves such that the stress ellipsoid transitions from a thin, elongated rod shape, gradually thickens, and may eventually become spherical in the case of isotropic turbulence (for graphical depiction refer to Fig. 1 in [26]).
- Closer to the blade, the turbulence primarily exhibits one-component (simple-shear) behavior. The RST quickly deforms and realigns, representing two-component turbulence. As the flow separates and is carried into the wake, the RST maintains its characteristics along streamlines, with a slight tendency towards returning to isotropy.

4.5 Uncertainty quantification

The modeled Reynolds stresses have been found to inadequately capture the physics of the problem. This has a direct impact on the turbulent kinetic energy production term. In the following analysis, we will explore the effects of constraining the modeled Reynolds stress tensor to specific turbulence limit states. This can be achieved utilizing the SU2 tool *EQUiPS* (Enabling Quantification of Uncertainty in Physics-based Simulations) proposed by Iaccarino et al. [27, 28]. The analysis starts expressing the perturbed Reynolds stress tensor as a function of its eigenvalues and eigenvectors:

$$R^\star_{ij} = 2k^\star \left(\frac{\delta_{ij}}{3} + v^\star_{ij} \Lambda^\star_{nl} v^\star_{lj} \right), \tag{19}$$

where $\star$ indicates perturbed quantities. The perturbations to the eigenvalues, Λ, correspond to varying the compositionality of the

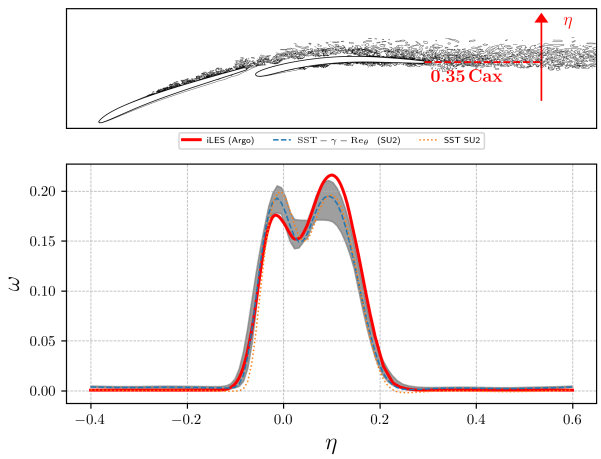

FIGURE 16: UNCERTAINTY QUANTIFICATION WITH EQUIPS

flow (or the shape of the Reynolds stress ellipsoid [14, 26]). The projection of the eigenvalue perturbation in the barycentric map has both a *direction* and a *magnitude*.

With respect to the direction of the eigenvalue perturbations, we focus on perturbations directed along the three vertices of the barycentric triangle: $\mathbf{x}_{1C}$, $\mathbf{x}_{2C}$, $\mathbf{x}_{3C}$, each representing a limiting state of Reynolds stress anisotropy. The magnitude of the perturbation in the barycentric triangle is represented by $\Delta_B \in [0, 1]$. Thus, $\Delta_B = 0$ leaves the state unperturbed, and $\Delta_B = 1.0$ perturbs to the vertices of the barycentric triangle.

The perturbed barycentric coordinates, $\mathbf{x}^*$, are given by:

$$\mathbf{x}^* = \mathbf{x} + \Delta_B \left(\mathbf{x}(t) - \mathbf{x}\right),$$

where $\mathbf{x}(t)$ denotes the target vertex (representing one of the one-, two-, or three-component limiting states), and $\mathbf{x}$ is the model prediction.

For the computations in this investigation, instead of relying on a user-defined magnitude for Δ_B, we set $\Delta_B = 1.0$, so that the three limiting states are considered. These are the default settings of this parameter, Δ_B, in the EQUiPS module and can be changed by the user.

Figure 16 illustrates the uncertainty band for the loss coefficient ω, shown in gray, which is obtained by perturbing the modeled Reynolds stress of the $SST - \gamma - Re_\theta$ model. These perturbations indirectly affect the production term of turbulent kinetic energy, resulting in variations in the energy dissipation mechanisms. While the WR-LES results are not entirely within this uncertainty band, they show closer agreement. This discrepancy can be attributed to the fact that not all sources of loss are solely associated with the modeled Reynolds stress tensor. Additionally, the perturbations are applied sequentially in different simulations, leading to an homogeneous variation of the turbulence state across the domain for each simulation.

5. CONCLUSION

The present study investigates compressor tandem blades from multiple perspectives, utilizing both wrLES and RANS approaches. In our analysis, wrLES demonstrates its value primarily in direct comparison with RANS. The back-to-back evaluation reveals several critical aspects of linear eddy-viscosity models that are particularly relevant from a design standpoint. The theoretical analyses here presented contribute to a deeper understanding of the tools commonly employed in daily engineering practice and pave the way for discussions on enhanced RANS models, which are expected to gain increasing prominence in the coming decades.

The wake of the front blade has been shown to play an active role in determining the overall dynamics of the cascade. The interaction with the boundary layer of the rear blade is a key factor, and unfortunately, it exhibits strong unsteady behavior, which is challenging to capture using RANS models. Consequently, high-performance design of tandem blades benefits more from scale-resolving simulations compared to single-blade configurations.

Another aspect is the transition on the front blade. This transition can be a persistent source of uncertainty, necessitating the use of specific transition models. These models are powerful tools, but they must be applied with care to avoid inaccuracies.

We discussed how the assumptions behind the linear eddy viscosity approach do not hold for this particular case. We believe this theoretical consideration may have broader implications. As an alternative, second-order closure models for this flow configuration will be explored in future work.

Our analysis of the turbulence state revealed an intricate dynamic that is extremely challenging to model accurately. AI-assisted CFD could aid in developing tailored closure models, requiring only a few high-fidelity simulations. However, significant progress is still needed before this approach becomes fully reliable.

In the meantime, we found that the uncertainty quantification techniques implemented in SU2 provide valuable insights into the uncertainty associated to RANS turbulence modeling. In our opinion, such tools deserve greater attention in applied CFD.

ACKNOWLEDGMENTS

The authors gracefully acknowledge the financial support of this work by the Walloon Region in Belgium through the Technological Innovation Partnership "Walloon Innovations for Green Skies" (WINGS, Contract No. 8441)

The present research benefited from computational resources made available on Lucia, the Tier-1 supercomputer of the Walloon Region, infrastructure funded by the Walloon Region under the grant agreement n°1910247.

REFERENCES

[1] Piomelli, Ugo and Balaras, Elias. "Wall-layer models for large-eddy simulations." *Annual Review of Fluid Mechanics* Vol. 34 (2008): pp. 349–374. URL https://api.semanticscholar.org/CorpusID:14097816.

[2] Georgiadis, Nicholas, Rizzetta, Donald and Fureby, Christer. "Large-Eddy Simulation: Current Capabilities, Recommended Practices, and Future Research." *AIAA Journal* Vol. 48 (2010): pp. 1772–1784. DOI 10.2514/1.J050232.

[3] Akolekar, Harshal D., Waschkowski, Fabian, Zhao, Yaomin, Pacciani, Roberto and Sandberg, Richard D. "Transition Modeling for Low Pressure Turbines Using Computa-

tional Fluid Dynamics Driven Machine Learning." *Energies* Vol. 14 No. 15 (2021). DOI 10.3390/en14154680.

[4] Wu, Jin-Long, Xiao, Heng and Paterson, Eric. "Physics-informed machine learning approach for augmenting turbulence models: A comprehensive framework." *Phys. Rev. Fluids* Vol. 3 (2018): p. 074602. DOI 10.1103/PhysRevFluids.3.074602.

[5] Gorlé, C., Zeoli, S., Emory, M., Larsson, J. and Iaccarino, G. "Epistemic uncertainty quantification for Reynolds-averaged Navier-Stokes modeling of separated flows over streamlined surfaces." *Physics of Fluids* Vol. 31 No. 3 (2019): p. 035101. DOI 10.1063/1.5086341.

[6] Konrath, Liesbeth and Peitsch, Dieter. "Impact of Tip Clearance Variation of Highly Loaded Tandem Blades in Axial Compressors." *Turbomachinery — Axial Flow Fan and Compressor Aerodynamics*, Vol. 13A: p. V13AT29A016. 2023. DOI 10.1115/GT2023-101865.

[7] Eckel, Jannik, Heinrich, Alexander, Janke, Christian, Ortmanns, Jens and Peitsch, Dieter. "3D Numerical and Experimental Investigation of High Turning Compressor Tandem Cascade." 2016.

[8] McGlumphy, Jonathan, Ng, Wing-Fai, Wellborn, Steven R. and Kempf, Severin. "Numerical Investigation of Tandem Airfoils for Subsonic Axial-Flow Compressor Blades." *Journal of Turbomachinery* Vol. 131 No. 2 (2009): p. 021018. DOI 10.1115/1.2952366.

[9] Schneider, Tim and Kožulović, Dragan. "Flow characteristics of axial compressor tandem cascades at large off-design incidence angles." *Turbo Expo: Power for Land, Sea, and Air*, Vol. 55225: p. V06AT35A011. 2013. American Society of Mechanical Engineers.

[10] Liu, Baojie, Zhang, Chuanhai, An, Guangfeng, Fu, Du and Yu, Xianjun. "Using tandem blades to break loading limit of highly loaded axial compressors." *Chinese Journal of Aeronautics* Vol. 35 No. 4 (2022): pp. 165–175. DOI https://doi.org/10.1016/j.cja.2021.07.031.

[11] Cockburn, Bernardo, Karniadakis, George and Eds, Shu. *Discontinuous Galerkin Methods: Theory, Computation and Application*. Vol. 11 (2000). DOI 10.1007/978-3-642-59721-3.

[12] Carton de Wiart, Corentin, Hillewaert, Koen, Bricteux, Laurent and Winckelmans, Gregoire. "Implicit LES of free and wall-bounded turbulent flows based on the discontinuous Galerkin/symmetric interior penalty method." *International Journal for Numerical Methods in Fluids* Vol. 78 (2015). DOI 10.1002/fld.4021.

[13] Palacios, Francisco, Colonno, Michael, Aranake, Aniket, Campos, Alejandro, Copeland, Sean, Economon, Thomas, Lonkar, Amrita, Lukaczyk, Trent, Taylor, Thomas and Alonso, Juan. "Stanford University Unstructured (SU2): An open-source integrated computational environment for multi-physics simulation and design." 2013. DOI 10.2514/6.2013-287.

[14] Pope, Stephen B. *Turbulent Flows*. Cambridge University Press (2000).

[15] Geuzaine, Christophe and Remacle, Jean-François. "Gmsh: A 3-D Finite Element Mesh Generator with Built-in Pre- and Post-Processing Facilities." *International Journal for Numerical Methods in Engineering* Vol. 79 (2009): pp. 1309 – 1331. DOI 10.1002/nme.2579.

[16] Menter, Florian, Langtry, RB and Völker, S. "Transition Modelling for General Purpose CFD Codes." *Flow, Turbulence and Combustion* Vol. 77 (2006): pp. 277–303. DOI 10.1007/s10494-006-9047-1.

[17] Langtry, Robin B. and Menter, Florian R. "Correlation-Based Transition Modeling for Unstructured Parallelized Computational Fluid Dynamics Codes." *AIAA Journal* Vol. 47 No. 12 (2009): pp. 2894–2906. DOI 10.2514/1.42362.

[18] "NASA Langley Research Center Turbulence Modeling Resource." https://turbmodels.larc.nasa.gov/index.html. Accessed: 2024-12-13.

[19] Menter, Florian, Kuntz, M. and Langtry, RB. "Ten years of industrial experience with the SST turbulence model." *Heat and Mass Transfer* Vol. 4 (2003).

[20] Rasquin, M, Bauer, A and Hillewaert, Koen. "Scientific post hoc and in situ visualisation of high-order polynomial solutions from massively parallel simulations." *International Journal of Computational Fluid Dynamics* (2019).

[21] Ovchinnikov, Victor, M., Choudhari Meelan and Piomelli, Ugo. "Numerical simulations of boundary-layer bypass transition due to high-amplitude free-stream turbulence." *Journal of Fluid Mechanics* Vol. 613 (2008): p. 135–169. DOI 10.1017/S0022112008003017.

[22] Wellinger, Philipp, Uhl, Philipp, Weigand, Bernhard and Rodriguez, Jose. "Analysis of turbulence structures and the validity of the linear Boussinesq hypothesis for an infinite tube bundle." *International Journal of Heat and Fluid Flow* Vol. 91 (2021): p. 108779. DOI https://doi.org/10.1016/j.ijheatfluidflow.2021.108779.

[23] Lumley, John L. and Newman, Gary R. "The return to isotropy of homogeneous turbulence." *Journal of Fluid Mechanics* Vol. 82 No. 1 (1977): p. 161–178. DOI 10.1017/S0022112077000585.

[24] S. Banerjee, F. Durst, R. Krahl and Zenger, Ch. "Presentation of anisotropy properties of turbulence, invariants versus eigenvalue approaches." *Journal of Turbulence* Vol. 8 (2007): p. N32. DOI 10.1080/14685240701506896. URL https://doi.org/10.1080/14685240701506896, URL https://doi.org/10.1080/14685240701506896.

[25] Emory, Michael and Iaccarino, Gianluca. "Visualizing turbulence anisotropy in the spatial domain with componentality contours." *Center for Turbulence Research. Annual Research Briefs 2014*. 2014. URL https://api.semanticscholar.org/CorpusID:29497825.

[26] Jofre, Lluís, Domino, Stefan P. and Iaccarino, Gianluca. "A Framework for Characterizing Structural Uncertainty in Large-Eddy Simulation Closures." *Flow, Turbulence and Combustion* Vol. 100 (2018): pp. 341–363. URL https://api.semanticscholar.org/CorpusID:125458935.

[27] Iaccarino, Gianluca, Mishra, Aashwin and Ghili, Saman. "Eigenspace perturbations for uncertainty estimation of single-point turbulence closures." *Physical Review Fluids* Vol. 2 (2017). DOI 10.1103/PhysRevFluids.2.024605.

[28] Thompson, Roney, Mishra, Aashwin, Iaccarino, Gianluca, Edeling, Wouter and Sampaio, Luiz. "Eigenvector perturbation methodology for uncertainty quantification of turbulence models." *Physical Review Fluids* Vol. 4 (2019). DOI 10.1103/PhysRevFluids.4.044603.